

Original Article

Tunable Na-doped MnO₂ Nanowires/g-C₃N₄ Composites for Efficient Energy Storage in Supercapacitors

Essa Mohammed J Alhelali¹, Ibrahim Asiri², Hassan Mohammed Almobarak³¹Department of Physics, College of Science, King Khalid University, Abha, Saudi Arabia,²Department of Asir Education Department, Ministry of Education, Abha, ASIR, Saudi Arabia,³CRCCSA-SAMA Consortium Site Office for Project Stadium and Surrounding Villages, Al Kurnaysh Br Rd, Jeddah, Saudi Arabia.

ABSTRACT

Objectives: This study aims to enhance the electrochemical performance of MnO₂-based supercapacitor electrodes by combining sodium (Na⁺) doping with graphitic carbon nitride (g-C₃N₄). The goal is to improve electrical conductivity, structural stability, ion-diffusion behavior, specific capacitance, and long-term cycling efficiency.

Material and Methods: Na-doped MnO₂ nanowires were synthesized using a hydrothermal method at 180 °C for 16 hours. g-C₃N₄ sheets were prepared by thermal annealing of melamine followed by ultrasonication. The Na-MnO₂/g-C₃N₄ composite was formed by sonicating Na-MnO₂ with exfoliated g-C₃N₄. Structural and morphological analyses were performed using X-ray diffraction (XRD), Fourier transform infrared spectroscopy (FTIR), scanning electron microscopy (SEM), Energy-Dispersive X-ray Spectroscopy (EDX), and Brunauer-Emmett-Teller (BET) surface area analysis. Electrochemical performance was evaluated in 1 M Na₂SO₄ electrolyte using cyclic voltammetry (CV), galvanostatic charge-discharge (GCD), and electrochemical impedance spectroscopy (EIS).

Results: The Na-MnO₂/g-C₃N₄ composite exhibited significantly improved electrochemical properties, achieving a specific capacitance of 953 F g⁻¹ at 1 A g⁻¹. It retained 89.83% of its capacitance at 9 A g⁻¹ and demonstrated excellent cycling stability with 96.2% capacitance retention after 6000 cycles at 12 A g⁻¹. EIS analysis showed reduced charge-transfer resistance and enhanced ionic/electronic conductivity compared with pristine MnO₂ and Na-MnO₂.

Conclusion: The synergistic integration of Na⁺ doping and g-C₃N₄ reinforcement significantly enhances the structural integrity and charge-storage capability of MnO₂ nanowires. The resulting composite shows high capacitance, strong rate capability, and outstanding long-term cycling stability, confirming its potential as a promising electrode material for next-generation supercapacitors.

Keywords: g-C₃N₄, MnO₂ NWs, Na doping, Supercapacitor

INTRODUCTION

Supercapacitors (SCs) are cutting-edge technology for addressing the global energy crisis, offering a balance of fast charge/discharge rates and long cycle life.^[1,2] Their high power density makes them perfect for application in hybrid electric vehicles and off-grid power systems. Nonetheless, their minimal energy density is a substantial obstruction to their widespread adoption. The equation $E = \frac{1}{2}CV^2$ explains how energy density is determined by both capacitance and the square of the potential window. As a consequence, boosting

energy density may be achieved by increasing the electrode material's capacitance or widening the potential window.^[3-5]

MnO₂ has emerged as a potential electrode material due to its eco-friendly nature, cost-effectiveness, and excellent theoretical capacitance (1370 F g⁻¹).^[6-8] Nevertheless, MnO₂ encounters low electrical conductivity (in the order of 10⁻⁶ S cm⁻¹) and limited energy density as well as power density.^[9,10] To address these bottlenecks, we intended to improve the electrical conductivity, energy density, and power density of MnO₂ through sodium doping. α-MnO₂ features a larger tunnel diameter (4.62 Å), facilitating the insertion and

*Corresponding author: Mr. Essa Mohammed J Alhelali, MSc Physics, Department of Physics, College of Science, King Khalid University, Abha, 61413, Saudi Arabia. ealhaly@kku.edu.sa

Received: 19 October 2025 Accepted: 11 January 2026 Epub Ahead of Print: 30 March 2026 Published: 08 May 2026 DOI: 10.25259/JQUS_22_2025

This is an open-access article distributed under the terms of the Creative Commons Attribution-Non Commercial-Share Alike 4.0 License, which allows others to remix, transform, and build upon the work non-commercially, as long as the author is credited and the new creations are licensed under the identical terms. ©2026 Published by Scientific Scholar on behalf of Journal of Qassim University for Science

extraction of ions.^[11,12] Water and larger ions (K⁺, Ag⁺, Na⁺) are excellent stabilizing agents for α -phase of MnO₂.^[13] Cation doping in the MnO₂ crystal can expedite ion transport. Na⁺ doping in MnO₂ has improved electrochemical performance. Zong *et al.* developed Na⁺-doped MnO₂ nanosheets that delivered a specific capacitance of 265.4 mF cm⁻².^[14] Jabeen *et al.* prepared Na⁺-pre-intercalated MnO₂ nanowalls, which retained 96% of their capacitance after 10000 cycles at a current density of 4 A g⁻¹.^[15]

Faradic reactions at or near the electrode surface may affect capacitance. Enhanced control over the morphology of electro-active materials provides a framework for improving surface and near-surface redox processes. One-dimensional (1-D) nanostructures, particularly nanowires (NWs), provide substantial benefits. NWs' morphology affords (i) rapid electrolyte ion movement and (ii) greater surface exposure thanks to deeper penetration of electrolyte ions, giving rise to improved contact between the electrode and electrolyte ions, resulting in decreased charging and discharging times.^[16,17] Additionally, these nanowires cope better with volume expansion, minimizing material deterioration and improving the cyclic life. NWs have a high aspect ratio, allowing charge carriers to travel only in one direction.^[18] Due to this feature, they are regarded as effective electrode materials, as the shorter ionic diffusion distance leads to higher charging and discharging rates. Mehmood *et al.* coupled ultrathin MnO₂ NWs with MXene, yielding a specific capacitance of 611.5 F g⁻¹ and 96% capacitance retention after 1,000 cycles.^[19] Raut *et al.* reported that MnO₂ NWs anchored on nickel foam (NF) delivered a specific capacitance of 641 F g⁻¹ at 2 A g⁻¹ with 97% capacitance retention.^[20] Yao *et al.* employed hydrothermal synthesis to manufacture ultralong α -MnO₂ NWs that delivered a specific capacitance of 118 F g⁻¹ at a 2 mV s⁻¹ sweep rate, along with 95.3% capacitance retention after 1,000 charging/discharging cycles.^[21]

To boost supercapacitor performance, N doping is recognized as an effective method for introducing additional active sites. The lone-pair electrons on N atoms induce negative charge on the carbon atoms in carbon-based compounds, improving their electrical conductivity.^[22] Graphitic carbon nitride (g-C₃N₄) has been explored for a number of applications, including supercapacitors, water splitting, and photocatalysis. Along with its economical production, g-C₃N₄ offers numerous advantages, including a large surface area, a unique electrical structure, an adequate band gap, exceptional chemical and thermal stability, and environmental friendliness.^[23] Its high electron-donating capacity, surface polarity, and enlarged electronic conductivity advance the electrochemical performance of materials. Additionally, g-C₃N₄ possesses a unique confined, conjugated framework

consisting of graphitic C₃N₄ layers linked by tertiary amines, which contribute to its high electronic conductivity.^[24,25]

Na⁺ doping and g-C₃N₄ doping advance the charge-storage efficiency of MnO₂ NWs. Na⁺ ions partially occupy the [2 × 2] tunnels of α -MnO₂, leading to minimal lattice expansion and reduced electrostatic repulsion within the tunnels. This structural modification reduces the ion-diffusion barrier, enabling faster insertion/extraction of electrolyte ions during cycling.^[26] Furthermore, Na⁺ doping strengthens the Mn-O framework by reducing Mn³⁺/Mn⁴⁺ disproportionation, thereby enhancing structural reversibility.^[27,28] Introducing g-C₃N₄ advances the electronic conductivity of the composite, advancing its overall efficiency. Wang *et al.* found that the π -conjugated structure of g-C₃N₄ enables effective electronic transport and close contact with MnO₂ NWs.^[29] This interconnected network enhances charge transfer, decreases resistance, and enables quicker electronic transport during redox processes.^[30] Thus, coupling Na⁺ doping with g-C₃N₄ enhances both ionic and electronic conductivity, resulting in high capacitance, exceptional rate capability, and prolonged cyclic life.^[31]

In this study, we optimized the electrochemical performance of MnO₂ supercapacitors via Na doping via the hydrothermal method. After Na doping, MnO₂ NWs were further reinforced by coupling with g-C₃N₄. The structural analysis of Na-MnO₂ and its composite with g-C₃N₄ is validated by X-ray diffraction (XRD), Fourier transform infrared spectroscopy (FTIR), scanning electron microscopy (SEM), Brunauer-Emmett-Teller (BET) surface area analysis. Cyclic voltammetry (CV), galvanostatic charge-discharge (GCD), and electrochemical impedance spectroscopy (EIS) analysis evaluated the electrochemical performance of electro-active materials. The as-prepared composite electrode material demonstrated improved conductivity, excellent cyclic stability, and outstanding specific capacitance. This enhanced performance is attributed to the morphology of Na-MnO₂ NWs, which offer a shorter diffusion path length, deep penetration of electrolyte ions, and increased conductivity and large surface area induced by g-C₃N₄. Therefore, this work aims to design and construct Na-doped MnO₂/g-C₃N₄ composite electrodes that combine high conductivity, a large surface area, and durable cyclic stability to achieve excellent supercapacitor performance.

Experimental

In this study, Na-MnO₂ nanowires were hydrothermally synthesized and subsequently integrated with exfoliated g-C₃N₄ sheets to form a conductive composite electrode.

MATERIAL AND METHODS

KMnO₄ (Sigma Aldrich, 99%), (NH₄)₂S₂O₈ (Daejung, 98%), HNO₃ (Sigma Aldrich, 70%), Na₂SO₄ (Daejung, 99%), C₂H₅OH (Sigma Aldrich, 99.9%), deionized water (DI water).

MnO₂ and Na-MnO₂ synthesis

A facile hydrothermal technique was employed to produce MnO₂ NWs, with and without sodium doping.^[32] First, 4 g of KMnO₄ were dissolved in DI water to create a homogeneous solution. Subsequently, 2 g of (NH₄)₂S₂O₈ were added, followed by 1 mL of HNO₃. The mixture was stirred for 30 min to ensure proper mixing. Once well mixed, the solution was poured into a 100 mL Teflon-lined autoclave heated to 180°C. The autoclave was then placed at this temperature for 16 h. After the reaction was complete, the autoclave was cooled to ambient temperature, and the precipitates were carefully recovered. These precipitates were completely free of impurities, neutralized, and dried at 100 °C. Na-MnO₂ NWs were prepared using the same preparation method by adding 340 mg of Na₂SO₄. The reaction conditions (180°C and 16 h) were selected based on earlier research and preliminary experiments that demonstrated that lower temperatures or shorter durations resulted in poor crystallinity and incomplete nanowire growth, while higher temperatures led to nanowire agglomeration.^[33]

g-C₃N₄ sheets synthesis

g-C₃N₄ was synthesized by annealing melamine for 2 h at 550 °C in a muffle furnace. The thereby formed g-C₃N₄ was finely ground in a mortar and pestle after cooling. The ground product was recognized as graphitic carbon nitride (g-C₃N₄). To prepare g-C₃N₄ sheets, the material was ultrasonicated for 5 h. The sonicated product was then dried at 80°C in an oven.^[34]

Na-MnO₂/g-C₃N₄ synthesis

To synthesize the Na-MnO₂/g-C₃N₄ composite, 20 mg of g-C₃N₄ was dissolved in DI water and sonicated for 30 min to achieve enough dispersion. The composite was prepared by adding 80 mg of Na-MnO₂ to the dispersed g-C₃N₄ solution and sonicating for 45 min. After the composite was thoroughly mixed, it was dried at 80°C. A schematic illustration of the synthesis of the Na-MnO₂ NWs/g-C₃N₄ composite is shown in Figure 1.

Electrode preparation

Electrodes of MnO₂, Na-MnO₂, and Na-MnO₂/g-C₃N₄ composites were fabricated for electrochemical performance evaluation without using any binder. The geometric area of each electrode was 1 cm² and was loaded with a mass of 6 mg

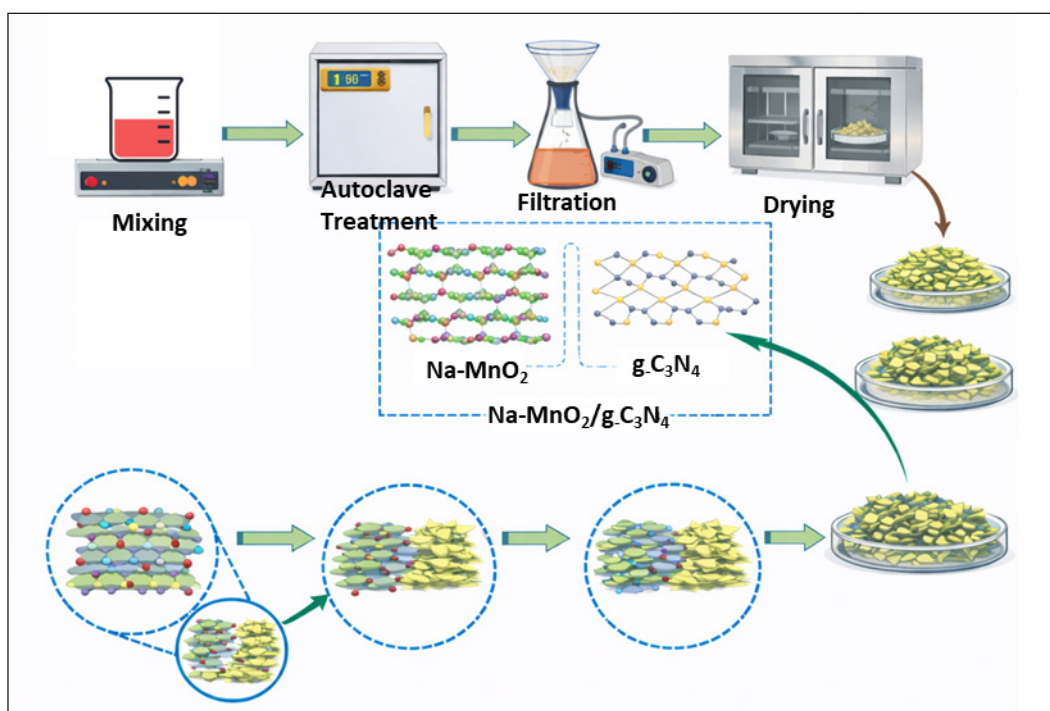


Figure 1: Schematic illustration for the synthesis of Na-MnO₂/g-C₃N₄ composite.

cm⁻². The electrochemical performance of these electrodes was explored in 1 M Na₂SO₄ aqueous electrolyte after deposition on nickel foam (NF). The active ingredient was sonicated for an hour in DI water to prepare a slurry. Afterwards, the paste was transferred to NF. After deposition, the drying was carried out at 60°C.

Characterization

A Philips X'Pert Pro X-ray diffractometer was employed for structural investigation, while an IR Affinity-1S spectrophotometer was utilized to determine functional groups. FEI Inspect S50 scanning electron microscope was used for morphological analysis, while elemental analysis was executed on JEOL JCM-6000 Plus SEM. Micromeritics ASAP 2020 Physisorption analyzer was utilized to measure the surface area. The Gamry interface 5000E was utilized for electrochemical performance evaluation. The BET surface area values were obtained from the MS Excel datasheet, and the pore size distribution was determined by plotting the relevant data in Origin. To extract equivalent circuit characteristics, data from electrochemical impedance spectroscopy (EIS) were fitted using EC-Lab software.

Electrochemical measurements

An electrochemical study was performed in a half-cell configuration. Ag/AgCl was used as the reference electrode, and a Pt wire was used as the counter electrode. The NF was used as a current collector. All measurements were performed in an aqueous solution of 1 M Na₂SO₄ as the electrolyte. Cyclic voltammetry (CV) and galvanostatic charge-discharge (GCD) measurements were performed in the potential range of 0-0.6 V. EIS measurements were made in the frequency range of 0.1 Hz to 0.1 MHz.

Table 1: Lattice parameters for MnO₂ and Na-MnO₂ NWs.

Sample	Crystallinity (%)	A (Å)	C (Å)	V (Å ³)	Crystallite size (nm)
MnO ₂	78	9.815	2.905	279.8	23
Na-MnO ₂	75	9.829	2.915	281.6	20

NWs: Nanowires

RESULTS AND DISCUSSION

XRD

XRD was employed to investigate the crystal structure of g-C₃N₄, MnO₂ NWs, Na-MnO₂ NWs, and Na-MnO₂ NWs/g-C₃N₄. Figure 2a depicts the XRD profile of all the samples, with 2θ at 12.53°, 17.89°, 25.56°, 28.35°, 37.42°, 41.62°, 49.53°, 56.60°, and 69.09°. According to ICDD card No. 00-044-0141,^[35] these peaks are ascribed to the (110), (200), (220), (310), (211), (301), (411), (600), (521), and (541) diffraction planes, respectively. The XRD profile confirmed that all MnO₂ samples are grown in the I4/m space group with a tetragonal structure. As displayed in Figure 2b, a change in peak position and reduction in intensity for Na-MnO₂ and Na-MnO₂/g-C₃N₄ were observed, which demonstrates the successful synthesis of doped and composite samples. This XRD peak shift towards lower 2θ values is associated with the larger ionic radii of the dopant, which expand the crystal lattice.^[36]

The crystallite size of bare and Na-doped MnO₂ NWs was calculated using the Debye-Scherrer equation.

$$D = \frac{K\lambda}{\beta \cos\theta} \quad (1)$$

The crystallite size of MnO₂ and Na-MnO₂ was calculated to be 23 nm and 20 nm, respectively. The crystallite size of

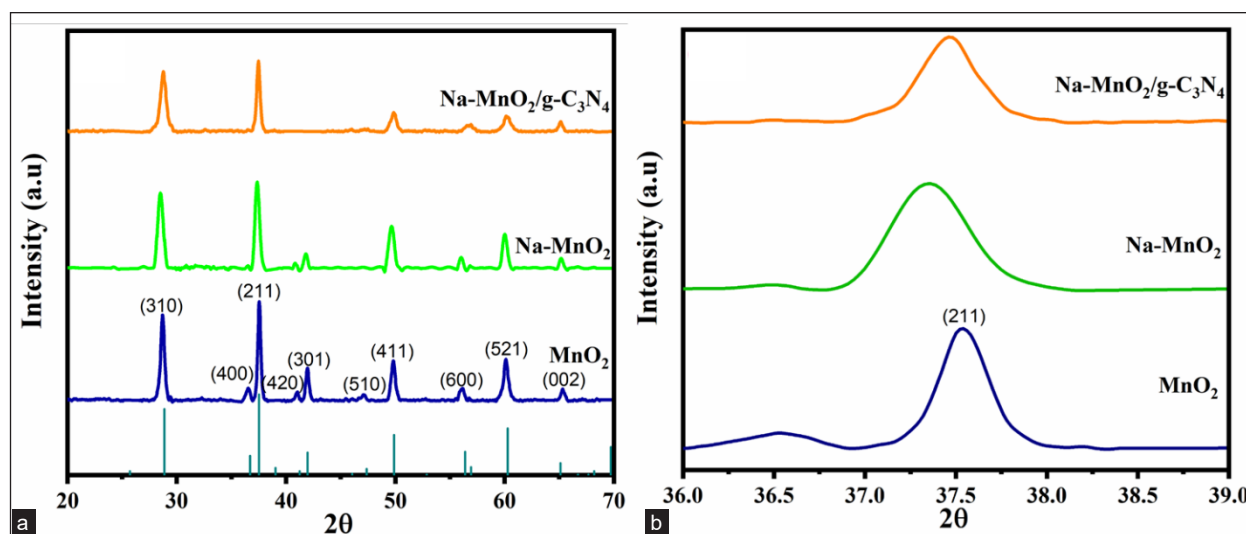


Figure 2: (a) XRD profile of all the samples, (b) Demonstration of XRD peak shifting with doping. (XRD: X-ray diffraction)

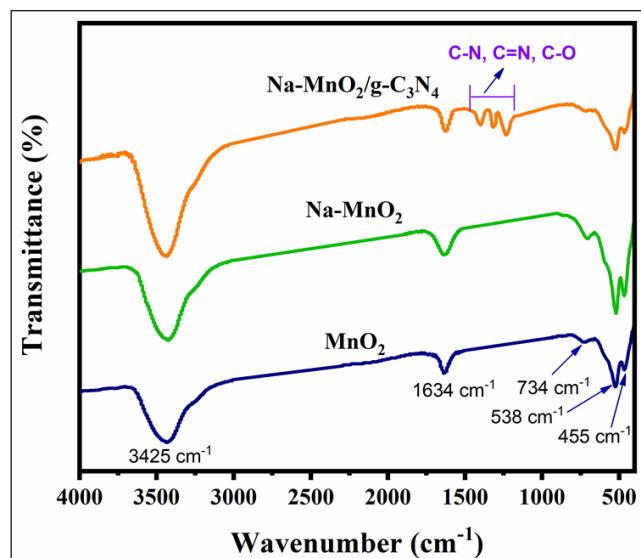


Figure 3: FTIR profile of the samples. (FTIR: Fourier transform infrared spectroscopy)

Na-doped MnO₂ NWs is reduced with respect to bare MnO₂ NWs. The greater ionic radii of the doped Na⁺ ions lead the crystallite lattice to expand, resulting in a decrease. Lattice parameters for MnO₂ and Na-MnO₂ NWs are given in Table 1.

FTIR

FTIR spectra of bare MnO₂ NWs and Na-MnO₂ NWs were recorded between 4000-400 cm⁻¹ and are shown in Figure 3. Five absorption bands have been found in bare MnO₂ NWs. The bands at 455 cm⁻¹, 538 cm⁻¹, and 734 cm⁻¹ correspond to Mn-O bonds of MnO₂, illustrating the successful synthesis of MnO₆ octahedra.^[32] The OH functional group from water adsorbed on the MnO₂ surface or within the tunnels accounts for the absorption band at 1634 cm⁻¹, which stabilizes the α -phase. A wide band at 3425 cm⁻¹ is ascribed to the O-H stretching vibration.^[37] The FTIR spectrum of Na-MnO₂ NWs

demonstrates similar absorption bands to bare MnO₂ NWs. However, with doping, the metal-oxygen (Mn-O) bands shift to lower wavenumbers, suggesting a weakening of the bond due to the stress induced in the crystal by Na doping. Na-MnO₂/g-C₃N₄ exhibited all characteristic absorption bands of Na-MnO₂, along with additional bands between 1175 cm⁻¹ and 1470 cm⁻¹ due to C-N, C=N, and C-O of g-C₃N₄.^[38] FTIR peak positions and their corresponding vibration modes are given in Table 2.

Table 2: FTIR peak positions and their corresponding vibration mode.

Sr. No.	Peak position (cm ⁻¹)	Vibration mode	Reference
1	455	Mn-O stretching	[39]
2	538	Mn-O stretching	[39]
3	734	Mn-O-Mn stretching	[39]
4	1175-1470	C-N, C-O, C=N	[40]
5	1634	OH bending	[41]
6	3425	OH stretching	[41]

FTIR: Fourier transform infrared spectroscopy

SEM

SEM has examined the morphologies of MnO₂, Na-MnO₂, g-C₃N₄, and Na-MnO₂/g-C₃N₄ composites. As shown in Figure 4a, the MnO₂ sample has grown into a 1-D NW morphology. The 1-D nano-architecture has an aspect ratio greater than 50 nm, making it best recognized as a nanowire. The majority of MnO₂ NWs are elongated, needle-like structures that are randomly interconnected, forming an irregular, mesh-like configuration. As shown in the Na-MnO₂ micrograph [Figure 4b], the doped NWs are uniformly dispersed and look randomly interwoven, demonstrating the fungal filaments' structure. SEM images of Na-MnO₂/g-C₃N₄ [Figure 4c] discovered that the synthesized Na-MnO₂ NWs have been incorporated in g-C₃N₄ sheets,

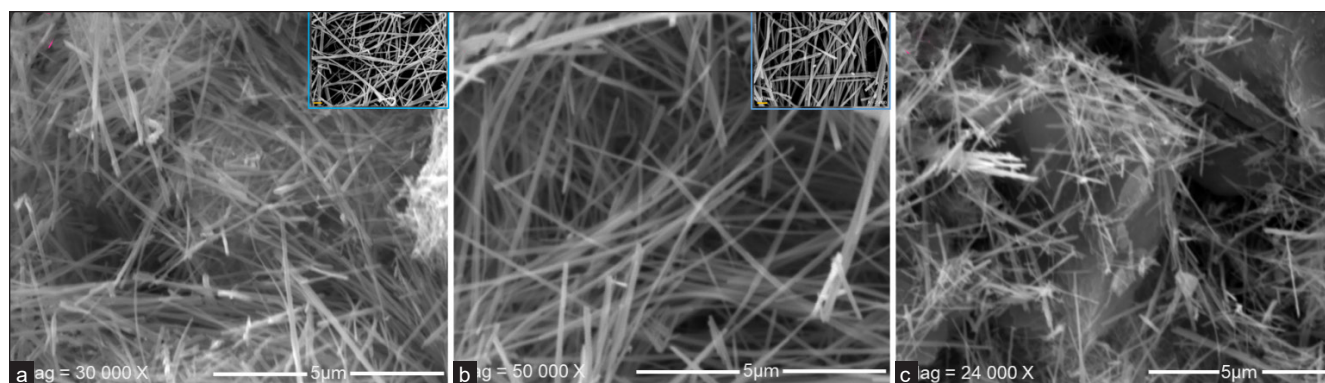


Figure 4: SEM micrographs of (a) MnO₂ (×30,000; inset: HRSEM image), (b) Na-MnO₂ (×50,000; inset: HRSEM image), (c) Na-MnO₂/g-C₃N₄ (×24,000). (SEM: Scanning electron microscopy; HRSEM: High resolution scanning electron microscopy)

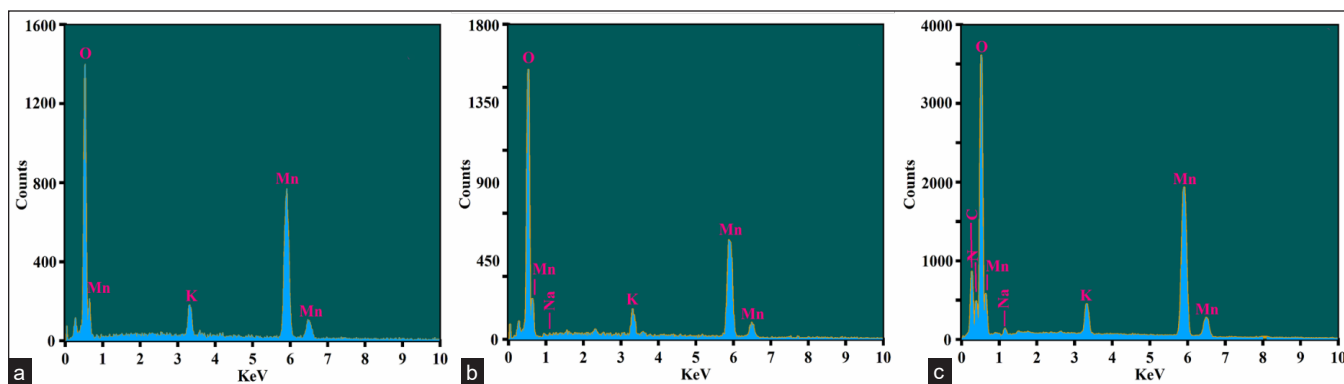


Figure 5: EDX profile of (a) MnO₂, (b) Na-MnO₂, (c) Na-MnO₂/g-C₃N₄. (EDX: Energy-Dispersive X-ray Spectroscopy)

Table 3: Elemental composition (atomic %) of all the samples.

Sample name	Mn (atomic %)	O (atomic %)	Na (atomic %)	C (atomic %)	N (atomic %)
MnO ₂	29.95	70.05	-	-	-
Na-MnO ₂	32.55	64.22	3.23	-	-
Na-MnO ₂ /g-C ₃ N ₄	31.25	46.35	2.99	10.75	8.66

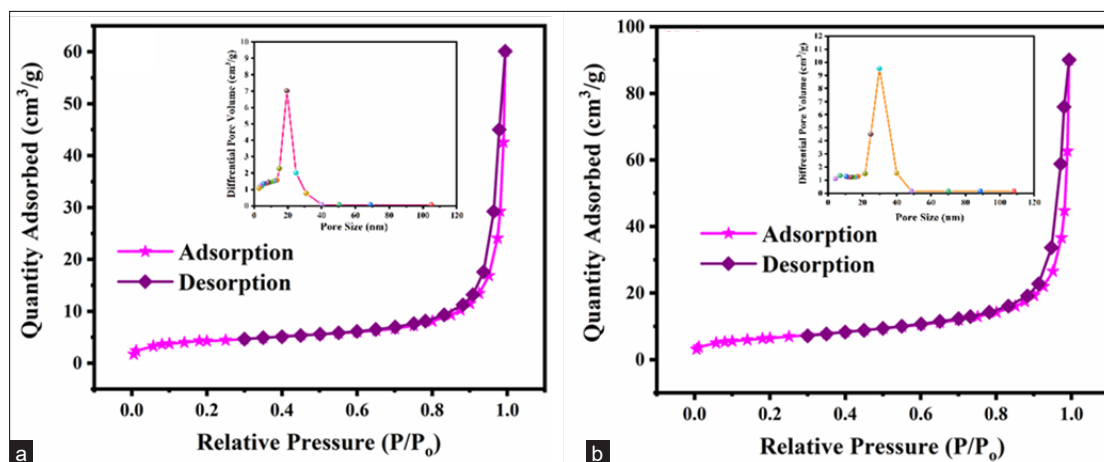


Figure 6: BET adsorption-desorption isotherm of (a) Na-MnO₂ (inset shows the pore size distribution), and (b) Na-MnO₂/g-C₃N₄ (inset shows the pore size distribution). (BET: Brunauer-Emmett-Teller surface area analysis)

confirming the preparation of the Na-MnO₂/g-C₃N₄ composite.

Elemental analysis

Energy-dispersive X-ray spectroscopy (EDX) has analyzed the prepared materials to determine their chemical purity and elemental composition. The EDX spectrum of the MnO₂ NWs [Figure 5a] demonstrated only peaks for oxygen and manganese, presenting the material's purity. The energy loss associated with electronic transitions from a higher-energy level to a lower-energy level (L/K shell) is measured in keV, with the K shell having a higher energy loss than the L shell. The EDX spectrum of the Na-MnO₂ NWs [Figure 5b]

presented extra peaks around 1 keV, which corresponded to the electronic de-excitation of the Na atom. The EDX pattern for Na-MnO₂/g-C₃N₄ [Figure 5c] displayed the existence of both Na-MnO₂ (Na, Mn, O) and g-C₃N₄ (C, N) components, indicating that the composite has been successfully synthesized. Elemental composition (atomic %) of all the samples is given in Table 3.

Surface area analysis

BET analysis was employed to explore Na-MnO₂ and Na-MnO₂ reinforced with g-C₃N₄, with a focus on the effect of g-C₃N₄ reinforcement on specific surface area. Figure 6 a and b shows the N₂ adsorption/desorption isotherms of

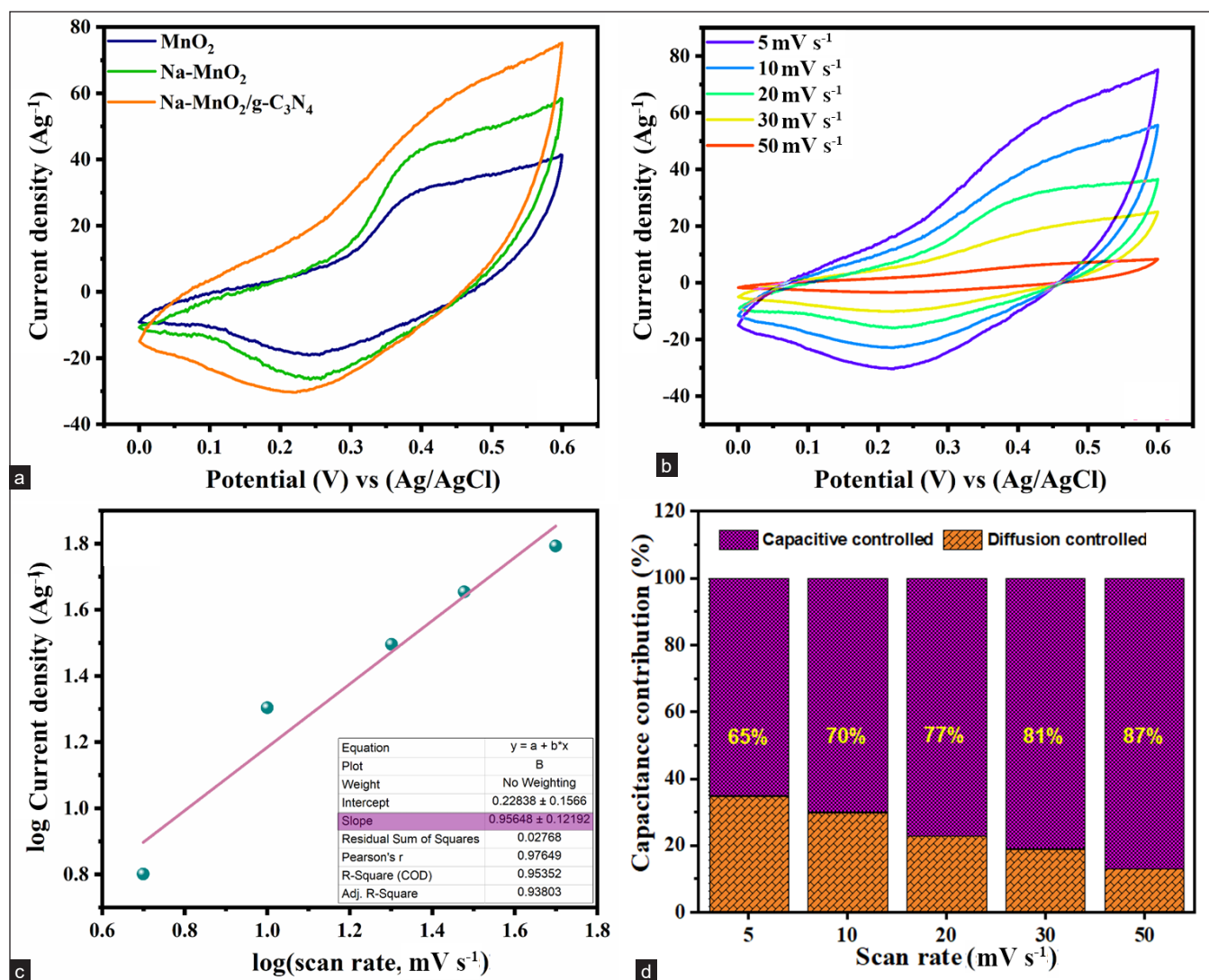


Figure 7: (a) CV profile of all the samples at 50 mV s^{-1} , (b) CV profile of Na-MnO₂/g-C₃N₄ @ various scan rates, (c) Power law plot to determine prominent charge storage process, (d) Capacitive-controlled and diffusion-controlled capacitance contribution towards total capacitance. (CV: Cyclic voltammetry, COD: Coefficient of determination)

the synthesized materials. Based on IUPAC standards, the isotherms for both samples are of type III, with H3 hysteresis loops. At elevated relative pressure, a rapid rise in adsorption across both profiles suggests small pores of the synthesized materials. Even though the adsorption behavior appears similar, the doped and composite samples demonstrated much greater gas adsorption than Na-MnO₂, indicating that metal doping and composite formation enhance surface area. The BET analysis showed specific surface areas of $55.2 \text{ m}^2 \text{ g}^{-1}$ for Na-MnO₂ and $85 \text{ m}^2 \text{ g}^{-1}$ for the g-C₃N₄-reinforced composite. Na-MnO₂ demonstrated a narrow mesoporous distribution positioned at 18-22 nm, generated by voids between MnO₂ nanowires [Figure 6a inset]. The Na-MnO₂/g-C₃N₄ composite demonstrated a wider mesoporous structure with bigger pores (25-35 nm), thanks to the spacer effect and

interfacial coupling of g-C₃N₄ nanosheets [Figure 6b inset]. This improved pore network enhances electrolyte penetration and ion-diffusion kinetics, leading to superior capacitance and rate performance for the composite electrode.

Electrochemical performance analysis

The electrochemical performance of MnO₂, Na-MnO₂, and the Na-MnO₂/g-C₃N₄ composite was evaluated by coating them onto NF to fabricate working electrodes. Key experiments, including CV, GCD, and Electrochemical Impedance Spectroscopy (EIS), were conducted at room temperature to assess the potential of the fabricated electrodes for supercapacitor applications. Figure 7a demonstrates the CV profiles for MnO₂ NWs, Na-MnO₂ NWs, and Na-MnO₂

NWs/g-C₃N₄ on NF at a scan rate of 50 mV s⁻¹. The appearance of oxidation and reduction peaks in the CV curves of bare and Na-MnO₂ electrodes specifies the presence of Faradaic redox processes. The CV curve area for Na-MnO₂ is larger than that of MnO₂, indicating a higher specific capacitance. Additionally, the CV profile of the Na-MnO₂/g-C₃N₄ electrode is relatively flat and symmetrical, indicating higher capacitance and a hybrid charge-storage mechanism.^[42] It is ascribed to the synergistic effect of Na-MnO₂ and g-C₃N₄, which has two components contributing to charge storage: electric double-layer capacitance (EDLC) from g-C₃N₄ and pseudocapacitive from Na-MnO₂. The predominant charge-storage mechanism in g-CN is EDLC.^[43]

Figure 7b displays the CV curves of Na-MnO₂/g-C₃N₄ obtained at scan rates from 5-50 mV s⁻¹. The material's excellent stability and reversible nature are demonstrated by the flatter CV curves at greater scan rates. This trend is apparent in the widening gap between the anodic and cathodic scans, along with the enlarged current responsiveness. Significantly, despite these variations, the overall shape of the CV curves remains consistent, confirming the stability of the Na-MnO₂/g-C₃N₄ material.

To identify the primary charge storage process (EDLC/Pseudocapacitive) in Na-MnO₂/g-C₃N₄ composite, a power law relationship $i=av^b$ was employed.^[44,45] A plot of the log of current density vs the log of scan rate, as shown in Figure 7c, was drawn to estimate the slope and intercept by linear fitting. A slope value of 0.5 indicates a diffusion-controlled process, whereas a slope value of 1 indicates a surface-controlled charge-transfer mechanism.^[46,47] In this study, the slope is 0.95, signifying that the surface-controlled process is dominant in Na-MnO₂/g-C₃N₄.

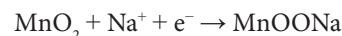
We employed Dunn's method to calculate the capacitive and diffusion-controlled capacitance (percentage) to total capacitance in Na-MnO₂/g-C₃N₄.^[48-50] The results are illustrated in Figure 7d. Across all feasible sweep rates, diffusion-controlled mechanisms made a much lesser contribution than surface-controlled mechanisms. At 5 mV s⁻¹, the diffusion-controlled mechanism had the highest contribution (35%), as slower sweep rates allow ions to permeate the active material's bulk or core. However, at 100 mV s⁻¹, the diffusion-controlled mechanism contributed only

S. No.	Sample	Surface area (m ² g ⁻¹)	Time (s)	Specific capacitance (F g ⁻¹)
1	MnO ₂	-	392	653
2	Na-MnO ₂	55.2	451	751
3	Na-MnO ₂ /g-C ₃ N ₄	85	561	935

Table 5: Specific capacitance of Na-MnO₂/g-C₃N₄ at different current densities.

S. No.	Current density (A g ⁻¹)	Discharging time (s)	Specific capacitance (F g ⁻¹)
1	1	561	935
2	3	180	900
3	5	106	883
4	7	73	851
5	9	56	840

13% to the total capacitance. At higher sweep rates, there is little time for deep electrolyte ion penetration, making the surface-dominated charge storage mechanism more prominent.^[32,51] The redox peaks of Na-MnO₂ and Na-MnO₂/g-C₃N₄ are due to reversible Mn³⁺/Mn⁴⁺ redox processes at the surface and near-surface regions. Na⁺ ions pre-intercalation enhances ion accessibility and subsurface penetration. Nevertheless, charge storage is still mostly through swift pseudocapacitive processes, not bulk intercalation. The charge storage process can be described as.



GCD behavior was explored on bare, sodium-doped, and g-C₃N₄-reinforced electrodes to obtain more accurate capacitance values. Figure 8a compares the GCD profiles of three electrodes at a current density of 1 A g⁻¹. Among these, the discharge time for Na-MnO₂/g-C₃N₄ (561 s) was longer than that of MnO₂ (392 s) and Na-MnO₂ (451 s). The accurate capacitance value for each electrode was calculated using Equation 2^[52] by using current density (I m⁻¹), discharging time (Δt) and potential window (ΔV).

$$C_{sp} = \frac{I \times \Delta t}{m \times \Delta V} \quad (2)$$

The Na-MnO₂/g-C₃N₄ electrode delivered a capacitance of 935 F g⁻¹, higher than the MnO₂ (653 F g⁻¹) and the Na-MnO₂ (751 F g⁻¹). As depicted in Figure 8a, the MnO₂ NWs endured an IR drop (or voltage drop) at the beginning of the discharging curve. The IR drop indicates the electrode's internal resistance.^[53] Sodium doping of MnO₂ reduced this IR loss, and the introduction of g-C₃N₄ practically eliminated it. This improvement is attributed to the synergistic effects of Na doping and g-C₃N₄ reinforcement, which enhance MnO₂ conductivity. The specific capacitance of all the samples is given in Table 4.

We further examined the composite-based electrode's behavior by calculating the specific capacitance of Na-MnO₂/g-C₃N₄ at various current densities. As demonstrated in Figure 8b, even when the current density progressively increases, the shape of the GCD curves remains

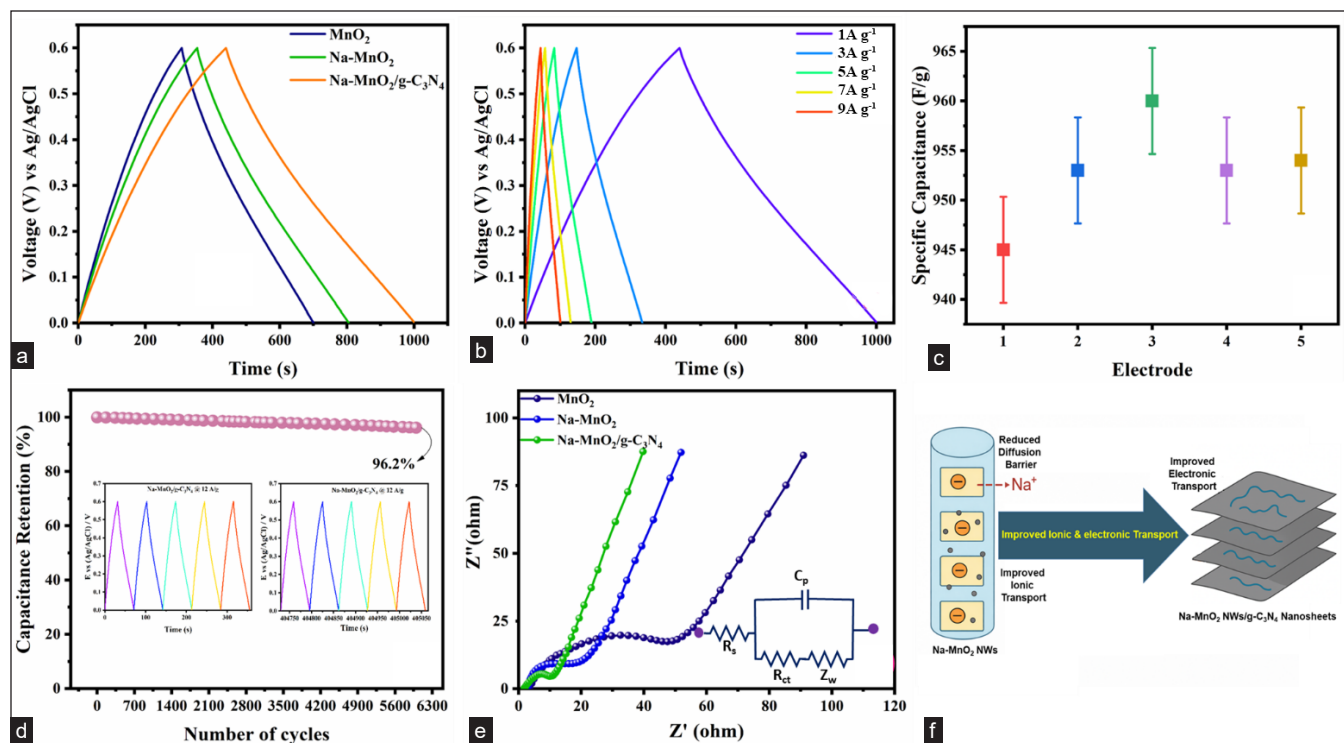


Figure 8: (a) GCD profile of all the samples, (b) GCD profile of Na-MnO₂/g-C₃N₄ @ various current densities, (c) Error bars for 5 different electrodes of Na-MnO₂/g-C₃N₄, (d) Cyclic performance of Na-MnO₂/g-C₃N₄ over 6000 cycles @ 12 A/g (inset: first 5 cycles and last 5 cycles), (e) EIS profile of all the samples (Inset shows the Randles circuit), (f) Graphical illustration of performance enhancement mechanism of Na-MnO₂ NWs/g-C₃N₄ nanosheets. (GCD: Galvanostatic charge–discharge; NWs: Nanowires)

S. No.	Sample	Solution resistance (R _s) (Ω)	Charge transfer resistance (R _{ct}) (Ω)
1	MnO ₂	3.58	44.29
2	Na-MnO ₂	2.71	14.69
3	Na-MnO ₂ /g-C ₃ N ₄	1.81	8.36

fundamentally the same, despite longer discharging times. This behavior determines the electrode material's astonishing stability through the charging/discharging cycles. The specific capacitance of Na-MnO₂/g-C₃N₄ was estimated by Equation 2, and the values are provided in Table 4. The Na-MnO₂/g-C₃N₄ delivered a specific capacitance of 953 F g⁻¹ at 1 A g⁻¹ and retained 89.83% of this value when tested at 9 A g⁻¹. The finding complies well with the anticipated rate performance. The decrease in capacitance at 9 A g⁻¹ is likely due to slower redox processes occurring at higher current densities. Particularly, at higher current densities, electrolyte ions endure less time to percolate into the material's bulk, causing them to reside on the surface, minimizing total capacitance predominantly. On the other hand, at a low current density of 1 A g⁻¹, the electrolyte ions

have sufficient time to percolate deeper into the electrode material, utilizing the bulk for charge storage and thereby enhancing capacitance. Specific capacitance of Na-MnO₂/g-C₃N₄ at different current densities is given in Table 5. Figure 8c shows the error bar profiles of specific capacitance for 5 different electrodes of the Na-MnO₂/g-C₃N₄ composite. One of the most important criteria determining how often a supercapacitor can be utilized is the cyclic stability of its electrode material. This measurement indicates a supercapacitor's potential to retain its original capacity after numerous charging/discharging cycles. The stability of the Na-MnO₂/g-C₃N₄ was assessed over 6000 GCD cycles at a current density of 12 A g⁻¹. As demonstrated in Figure 8d, the Na-MnO₂/g-C₃N₄ possesses outstanding cycling stability by keeping 96.2% of its capacitance after 6000 cycles.

EIS analysis provides information on the various obstacles an electrode encounters when an AC flows through it. The Nyquist plot is drawn by plotting the real and imaginary components along the x- and y-axes for bare MnOO₂, Na-MnO₂, and Na-MnO₂/g-C₃N₄ composite electrodes, respectively. The Nyquist plots for all three samples are illustrated in Figure 8e. Three sections in a Nyquist plot are usually observed: (i) the x-intercept; (ii) a semicircular diameter; and (iii) a diagonal

Table 7: Electrochemical performance comparison of Na-MnO₂/g-C₃N₄ with previously reported MnO₂-based electrodes.

Electrode material	Specific capacitance	Current density	Cyclic activity (%) / No. of cycles	Reference
MnO ₂ /Ti ₃ C ₂ T _x	462.8 F g ⁻¹	1 A g ⁻¹	81/5000	[55]
V ₂ O ₅ /MnO ₂	219 F g ⁻¹	1 A g ⁻¹	97/6500	[56]
Na-MnO ₂	655 F g ⁻¹	1 A g ⁻¹	95/4000	[57]
g-C ₃ N ₄ /MnO ₂	555 F g ⁻¹	1 A g ⁻¹	91.74/2000	[58]
KNa-MnO ₂	361 F g ⁻¹	1 A g ⁻¹	116/2000	[59]
Na-MnO ₂	324.7 F g ⁻¹	0.5 A g ⁻¹	91/10000	[60]
Na-MnO ₂ /g-C ₃ N ₄	953 F g ⁻¹	1 A g ⁻¹	96.2/6000	This Work

line.^[54] The Nyquist plot for the bare MnO₂ shows a broader semicircle with a larger x-intercept, indicating higher charge transfer resistance (R_{ct}) and solution resistance (R_s). The Na-MnO₂ shows a smaller semicircle and a smaller x-intercept, indicating improved electrical conductivity due to Na doping. The Na-MnO₂/g-C₃N₄ exhibits the smallest semicircle and the x-intercept closest to the origin, indicating low resistance and efficient charge and mass transfer. The resistance values of all the samples are given in Table 6.

Na⁺ ions occupy the tunnels of the MnO₂ lattice, which leads to lattice expansion and deformation, generating extra defect sites and oxygen vacancies. These modifications enhance ionic conductivity through rapid Na⁺ ion diffusion and electrical conductivity by increasing the charge-carrier density. Additionally, Na⁺ doping strengthens MnO₂, thereby enhancing electrochemical stability. The introduction of g-C₃N₄ enhances charge transfer by serving as a conductive, chemically stable 2D support. The π-conjugated structure of g-C₃N₄ facilitates electronic transport and establishes a close interfacial contact with Na-MnO₂, thereby decreasing charge-transfer resistance. Thus, combining these two distinctive features in a single electrode material has improved overall supercapacitor performance. A graphical illustration of the performance enhancement mechanism of Na-MnO₂ NWs/g-C₃N₄ nanosheets is shown in Figure 8f. A comparison of the specific capacitance of Na-MnO₂/g-C₃N₄ with previously reported values is shown in Table 7.

CONCLUSION

In conclusion, MnO₂ NWs and Na-MnO₂ NWs have been successfully synthesized by hydrothermal treatment followed by the synthesis of Na-MnO₂/g-C₃N₄ composite via ultrasonication. The composite material delivered a high specific capacitance of 953 F g⁻¹ at 1 A g⁻¹, decent rate capability (89.83% retention at 9 A g⁻¹), and excellent long-term cycling

stability (96.2% capacitance retention after 6000 cycles at a current density of 12 A g⁻¹). Na doping and the incorporation of g-C₃N₄ reduced the charge transfer resistance, as revealed by EIS measurements. These results highlight the synergistic effect of Na doping and g-C₃N₄ incorporation, demonstrating a viable strategy to improve the energy storage capability of modified MnO₂ electrodes for supercapacitor applications. This work opens new horizons for high-performance supercapacitor applications in versatile, portable devices and in next-generation energy storage systems.

Author's contribution: EMA: Supervision, conceptualization, methodology, formal analysis, investigation, project administration, resources; IA: Writing – original draft, writing – review & editing, software, methodology, formal analysis, data curation; HMA: Visualization, validation, investigation.

Ethical approval: Institutional Review Board approval is not required.

Declaration of patient consent: Patient consent is not required as no patients are involved in the study.

Financial support and sponsorship: Nil.

Conflicts of interest: There are no conflicts of interest.

Use of artificial intelligence (AI)-assisted technology for manuscript preparation: The authors confirm that there was no use of artificial intelligence (AI)-assisted technology for assisting in the writing or editing of the manuscript and no images were manipulated using AI.

REFERENCES

- Shin J, Tran VH, Tien Nguyen DC, Kim SK, Lee S-H. Integrated photo-rechargeable supercapacitors formed via electrode sharing. *Org Electron* 2021;89:106050.
- Singh N, Singh V, Bisht N, Negi P, Dhyani A, Sharma RK, *et al.* A comprehensive review on supercapacitors: Basics to recent advancements. *J Energy Storage* 2025;121:116498.
- Shi P, Li L, Hua L, Qian Q, Wang P, Zhou J, *et al.* Design of amorphous manganese oxide@multiwalled carbon nanotube fiber for robust solid-state supercapacitor. *ACS Nano* 2017;11:444-52.
- Zhai T, Wan L, Sun S, Chen Q, Sun J, Xia Q, *et al.* Phosphate ion functionalized Co₃O₄ ultrathin nanosheets with greatly improved surface reactivity for high performance pseudocapacitors. *Adv Mater* 2017;29:1604167. <https://doi.org/10.1002/adma.201604167>
- Hasegawa G, Kanamori K, Kiyomura T, Kurata H, Abe T, Nakanishi K. Hierarchically porous carbon monoliths comprising ordered mesoporous nanorod assemblies for high-voltage aqueous supercapacitors. *Chem Mater* 2016;28:3944-50.
- Cui M, Kang L, Shi M, Xie L, Wang X, Zhao Z, *et al.* Explore the influence of agglomeration on electrochemical performance of an amorphous MnO₂/C composite by controlling drying process. *Appl Surface Sci* 2017;416:241-7.
- Yuan Y, Zhu J, Wang Y, Li S, Jin P, Chen Y. Facile synthesis of manganese oxide nanostructures with different crystallographic

- phase and morphology for supercapacitors. *J Alloys Compd* 2020;830:154524.
8. Obeidat AM. Solid-state supercapacitors based on poly (3, 4-ethylenedioxythiophene) (PEDOT) – manganese oxide (MnO₂) composite electrodes synthesized by single-step co-deposition for electrical energy storage. *Mater Today Energy* 2018;10:81-8.
 9. Zhao J, Liu X, Liu P, Deng K, Lv X, Tian W, *et al.* Oxygen vacancies refilling and potassium ions intercalation of δ -manganese dioxide with high structural stability toward 2.3 V high voltage asymmetric supercapacitors. *J Colloid Interface Sci* 2023;629:1039-48.
 10. Song X, Wang H, Li Z, Du CF, Guo R. A review of MnO₂ composites incorporated with conductive materials for energy storage. *Chem Rec* 2022;22:e202200118.
 11. Song Z, Yan Z, Yang X, Bai H, Duan Y, Yang B, *et al.* First principles density functional theory study of Pb doped α -MnO₂ catalytic materials. *Chem Phys Lett* 2018;695:216-21.
 12. Lambert TN, Vigil JA, White SE, Delker CJ, Davis DJ, Kelly M, *et al.* Understanding the effects of cationic dopants on α -MnO₂ oxygen reduction reaction electrocatalysis. *J Phys Chem C* 2017;121:2789-97.
 13. Xiong T, Tan TL, Lu L, Lee WSV, Xue J. Harmonizing energy and power density toward 2.7 V asymmetric aqueous supercapacitor. *Adv Energy Mater* 2018;8:1702630.
 14. Zong Q, Zhang Q, Mei X, Li Q, Zhou Z, Li D, *et al.* Facile synthesis of Na-doped MnO₂ nanosheets on carbon nanotube fibers for ultrahigh-energy-density all-solid-state wearable asymmetric supercapacitors. *ACS Appl Mater Interfaces* 2018;10:37233-41.
 15. Jabeen N, Hussain A, Xia Q, Sun S, Zhu J, Xia HJA. High-performance 2.6 V aqueous asymmetric supercapacitors based on in situ formed Na_{0.5}MnO₂ nanosheet assembled nanowall arrays. *Adv Mater* 2017;29:1700804.
 16. Chan CK, Peng H, Liu G, McIlwrath K, Zhang XF, Huggins RA, *et al.* High-performance lithium battery anodes using silicon nanowires. *Nat Nanotechnol* 2008;3:31-5.
 17. Chen HM, Chen CK, Liu RS, Zhang L, Zhang J, Wilkinson DP. Nano-architecture and material designs for water splitting photoelectrodes. *Chem Soc Rev* 2012;41:5654-71.
 18. Lu X, Zhang W, Wang C, Wen T-C, Wei Y. One-dimensional conducting polymer nanocomposites: Synthesis, properties and applications. *Prog Polym Sci* 2011;36:671-712.
 19. Mahmood M, Rasheed A, Ayman I, Rasheed T, Munir S, Ajmal S, *et al.* Synthesis of ultrathin MnO₂ nanowire-intercalated 2D-MXenes for high-performance hybrid supercapacitors. *Energy Fuels* 2021;35:3469-78.
 20. Raut SD, Mane HR, Shinde NM, Lee D, Shaikh SF, Kim KH, *et al.* Electrochemically grown MnO₂ nanowires for supercapacitor and electrocatalysis applications. *N J Chemistry* 2020;44:17864-70.
 21. Yao W, Wang J, Li H, Lu Y. Flexible α -MnO₂ paper formed by millimeter-long nanowires for supercapacitor electrodes. *J Power Sources* 2014;247:824-30.
 22. Kavil J, Anjana PM, Periyat P, Rakhi RB. One-pot synthesis of g-C₃N₄/MnO₂ and g-C₃N₄/SnO₂ hybrid nanocomposites for supercapacitor applications. *Energy & Fuels* 2018;2:2244-51.
 23. Bhandari D, Lakhani P, Modi CK. Graphitic carbon nitride (g-C₃N₄) as an emerging photocatalyst for sustainable environmental applications: A comprehensive review. *RSC Sustain* 2024;2:265-87.
 24. Kalidasan K, Mallapur S, Munirathnam K, Nagarajaiah H, Reddy MBM, Kakarla RR, *et al.* Transition metals-doped g-C₃N₄ nanostructures as advanced photocatalysts for energy and environmental applications. *Chemosphere* 2024;352:141354.
 25. Cao S, Yu J. G-C₃N₄-based photocatalysts for hydrogen generation. *J Phys Chem Lett* 2014;5:2101-7.
 26. Quinzeni I, Fujii K, Bini M, Yashima M, Tealdi C. Na⁺ diffusion mechanism and transition metal substitution in tunnel-type manganese-based oxides for Na-ion rechargeable batteries. *Adv Mater* 2022;3:986-97.
 27. Le T. Optimization of low-toxicity manganese-based layered oxides for sodium-ion batteries through doping and surface coating techniques. Bachelor's thesis. Espoo, Finland: Aalto University; 2025;245.
 28. Huang X, Li D, Huang H, Jiang X, Yang Z, Zhang W. Fast and highly reversible Na⁺ intercalation/extraction in Zn/Mg dual-doped P2-Na_{0.67}MnO₂ cathode material for high-performance Na-ion batteries. *Nano Res* 2021;14:3531-7.
 29. Wang X, Maeda K, Thomas A, Takanabe K, Xin G, Carlsson JM, *et al.* A metal-free polymeric photocatalyst for hydrogen production from water under visible light. *Nat Mater* 2009;8:76-80.
 30. Ong WJ, Tan LL, Ng YH, Yong ST, Chai SP. Graphitic carbon nitride (g-C₃N₄)-based photocatalysts for artificial photosynthesis and environmental remediation: Are we a step closer to achieving sustainability? *Chem Rev* 2016;116:7159-329.
 31. Liu J, Bao J, Zhang X, Gao Y, Zhang Y, Liu L, *et al.* MnO₂-based materials for supercapacitor electrodes: Challenges, strategies and prospects. *RSC Adv* 2022;12:35556-78.
 32. Khalid MU, Zulfiqar S, Khan MN, Shakir I, Warsi MF, Cochran EW. Electrochemical performance enhancement of MnO₂ nanowires through silver incorporation for next-generation supercapacitors. *Adv Mater* 2024;5:6170-84.
 33. Khalid MU, Zulfiqar S, Warsi MF, Shakir I, Al-Buriahi MS, Cochran EW. Investigating the influence of sodium preintercalation on the electrochemical behavior of ultrathin MnO₂ nanowires for enhanced supercapacitor performance. *Energy Fuels* 2024;38:5506-21.
 34. Alalawi A, Romman UE, Katubi KM, Shafa S, Usman Khalid M, Alrowaili ZA, *et al.* Ag-doped MnO₂ nanowires integrated with graphitic carbon nitride for enhanced photocatalytic applications for waste water treatment. *Curr Appl Phys* 2024;60:32-42.
 35. Pathak YA, Mane AT, More PD, Thube SGJC. Controlled hydrothermal growth of α -MnO₂ nanorods: Effect of temperature on electrochemical performance. *Chem Select* 2025;10:e04076.
 36. Bashir B, Khalid MU, Aadil M, Zulfiqar S, Warsi MF, Agboola PO, *et al.* CuxNi1-xO nanostructures and their nanocomposites with reduced graphene oxide: Synthesis, characterization, and photocatalytic applications. *Ceram Int* 2021;47:3603-13.
 37. Khalid MU, Huwayz MA, Zulfiqar S, Cochran EW, Alrowaili ZA, Al-Buriahi MS, *et al.* Phase transformation of α -MnO₂ to

- β - MnO₂ induced by Cu doping: Improved electrochemical performance for next generation supercapacitor. *Mater Sci Eng B* 2023;295:116580.
38. Shaheen N, Waqas M, Alazmi A, Alkhudhayri AA, Hasan M, Shahid M, *et al.* Hydrothermal assisted WO₃@C nanowires supported g-C₃N₄ ternary nanocomposites for the removal of colored and colorless organic effluents and bacterial strains. *Mater Chem Phys* 2022;292:126754.
 39. Wang H, Lu Z, Qian D, Li Y, Zhang WJN. Single-crystal α -MnO₂ nanorods: Synthesis and electrochemical properties. *Nanotechnol* 2007;18:115616.
 40. Shaheen N, Waqas M, Alazmi A, Alkhudhayri AA, Hasan M, Shahid M, *et al.* Hydrothermal assisted WO₃@C nanowires supported g-C₃N₄ ternary nanocomposites for the removal of colored and colorless organic effluents and bacterial strains. *Mater Chem Phys* 2022;292:126754.
 41. Ananth MV, Pethkar S, Dakshinamurthi K. Distortion of MnO₆ octahedra and electrochemical activity of nstutite-based MnO₂ polymorphs for alkaline electrolytes-an FTIR study. *J Power Sources* 1998;75:278-82.
 42. Karimi-Maleh H, Afşin Kariper İ, Karaman C, Korkmaz S, Karaman O. Direct utilization of radioactive irradiated graphite as a high-energy supercapacitor a promising electrode material. *Fuel* 2022;325:124843.
 43. Arora R, Dhanda M, Malik R, Ahlawat S, Yadav M, Nehra SP, *et al.* Graphitic carbon nitride and graphene electrodes for supercapacitors' energy accretion: A progressive excerpt. *Eur Polym J* 2023;201:112552.
 44. Yang C, Hong L, Chong P, Li Y, Wei M. Tin-based metal-phosphine complexes nanoparticles as long-cycle life electrodes for high-performance hybrid supercapacitors. *J Colloid Interface Sci* 2022;606:148-57.
 45. Shafi I, Liang E, Li B. Ultrafine chromium oxide (Cr₂O₃) nanoparticles as a pseudocapacitive electrode material for supercapacitors. *J Alloys Compd* 2021;851:156046.
 46. Yu F, Huang T, Zhang P, Tao Y, Cui FZ, Xie Q, *et al.* Design and synthesis of electrode materials with both battery-type and capacitive charge storage. *Energy Storage Mater* 2019;22:235-5.
 47. Okpara EC, Fayemi OE, Sherif ESM, Ganesh PS, Swamy BEK, Ebenso EE. Electrochemical evaluation of Cd²⁺ and Hg²⁺ ions in water using ZnO/Cu₂ONPs/PANI modified SPCE electrode. *Sens Biosensing Res* 2022;35:100476.
 48. Shao H, Lin Z, Xu K, Taberna P-L, Simon P. Electrochemical study of pseudocapacitive behavior of Ti₃C₂Tx MXene material in aqueous electrolytes. *Energy Storage Mater* 2019;18:456-61.
 49. Anjana R, Anjana PM, Alex J, Isaac R, Hussain RSS, Sajan D. Investigations on supercapacitor performance of novel ZnO-CeO₂-rGO nanohybrid prepared via hydrothermal method for energy storage applications and their charge storage mechanism. *Diam Relat Mater* 2024;146:111241.
 50. Cheng C, Lai G. Supercapacitor behavior of nano-Fe₂(MoO₄)₃. *Mater Lett* 2021;301:130246.
 51. Liu Y, Jiang S.P, Shao Z. Intercalation pseudocapacitance in electrochemical energy storage: Recent advances in fundamental understanding and materials development. *Mater Today Adv* 2020;7:100072.
 52. Sethi M, Shenoy US, Bhat DK. A porous graphene-NiFe₂O₄ nanocomposite with high electrochemical performance and high cycling stability for energy storage applications. *Nanoscale Adv* 2020;2:4229-41.
 53. Oliveira RD, Santos CS, Garcia JR, Vidotti M, Marchesi LF, Pessoa CA. IR drop studies of poly(aniline)-based modified electrodes. *J Electroanal Chem* 2020;878:114662.
 54. Kumar Y, Chopra S, Gupta A, Kumar Y, Uke SJ, Mardikar SP. Low temperature synthesis of MnO₂ nanostructures for supercapacitor application. *Mater Sci Energy Technol* 2020;3:566-74.
 55. Wang Z, Zhang D, Guo Y, Jiang H, Wang D, Cheng J, *et al.* Ti₃C₂Tx MXene-embedded MnO₂-based hydrophilic electrospun carbon nanofibers as a freestanding electrode for supercapacitors. *Chem Commun(Camb)* 2023;59:14309-12.
 56. R R, Thejas Prasannakumar A, V M, Varma SJ. V₂O₅/MnO₂ nanostructured electrodes for high-energy-density supercapacitors. *ACS Appl Nano Mater* 2025;8:13861-75.
 57. Wang K, Wang J, Qian J, Yu Q, Bai JQ, Wei Y, *et al.* Boosted Na⁺-MnO₂ supercapacitor performance via strong metal support interaction. *J Colloid Interface Sci* 2025;682:865-74.
 58. Santhosh PC, Jayakumar S, Radhamani AV. Engineered S-scheme g-C₃N₄/MnO₂ heterostructures for integrated photo-rechargeable supercapacitors with enhanced energy storage performance. *Nanoscale* 2026;18:351-65.
 59. Vashisth P, Sharma A, Nasit M, Singh JP, Anjali N, Varshney M, *et al.* Fabrication of Na and K based MnO₂ nanocomposites for supercapacitive applications. *Heliyon* 2024;10:e35360.
 60. Bai H, Liang S, Wei T, Zhou Q, Shi M, Jiang Z, *et al.* Enhanced pseudo-capacitance and rate performance of amorphous MnO₂ for supercapacitor by high Na doping and structural water content. *J Power Sources* 2022;523:231032.

How to cite this article: Alhelali EMJ, Asiri I, Almobarak HM. Tunable Na-doped MnO₂ Nanowires/g-C₃N₄ Composites for Efficient Energy Storage in Supercapacitors. *J Qassim Univ Sci.* 2026;2:202-13. doi: 10.25259/JQUS_22_2025.